Fuel temperature and injection pressure influence on the cold start GDI sprays

Kyungwon Lee [a], Dario Lopez Pintor [b], Dimitris Assanis [c], Seokwon Cho [d,e], Joonsik Hwang [a,e,f,*]

[a] Department of Mechanical Engineering, Mississippi State University, Mississippi State, MS 39762, USA
[b] Combustion Research Facility, Sandia National Laboratories, Livermore, CA 94550, USA
[c] Department of Mechanical Engineering, Stony Brook University, Stony Brook, NY 11794, USA
[d] Department of Aerospace Engineering, Mississippi State University, Mississippi State, MS 39762, USA
[e] Center for Advanced Vehicular Systems (CAVS), Mississippi State University, Starkville, MS 39759, USA
[f] Institute for Clean Energy Technology (ICET), Mississippi State University, Starkville, MS 39759, USA

ARTICLE INFO

ABSTRACT

Cold start in gasoline direct injection engines (GDI) is a critical issue that significantly impacts fuel consumption and emissions. Therefore, it is essential to investigate and improve the spray and air-fuel mixing processes during cold starts. This study employed a complimentary set of optical diagnostic techniques, including line-of-sight (extinction, Schlieren, and long-distance microscopy) and 3D computed tomography (CT), to characterize and understand the cold-start spray dynamics under various fuel temperature and injection pressure conditions. The experiments were conducted in a constant volume spray vessel and the fuel temperature was varied using a coolant circulator, with temperatures reaching as low as -7 °C to simulate cold-start conditions. The cold fuel exhibited longer liquid/vapor penetration lengths compared to hot fuel under low injection pressure conditions. This deterioration in spray characteristics was attributed to the attenuated fuel evaporation and reduced entrainment of ambient air. The 3D spray visualization obtained through the CT algorithm, particularly the cut plane images, revealed that plumes with low fuel temperatures had narrower individual plume widths, resulting in minimized plume-to-plume interaction. Microscopic imaging further confirmed this observation which showed separate plumes in the near-nozzle region for cold fuel conditions. Meanwhile, hot fuel under high injection pressure conditions exhibited complete plume collapsing, leading to a significant amount of liquid fuel remaining in the spray core. The liquid penetration reached 70 mm during the injection period, potentially can cause wall wetting on the piston top or cylinder wall. Based on the experimental findings, this study suggests the application of multiple injections with a moderate level of injection pressure for optimized engine performance and reduced emissions during cold starts.

Introduction

In recent decades, gasoline engines have undergone significant advancements to meet increasingly stringent emissions and fuel efficiency regulations. One notable innovation in gasoline engine technology is the adoption of direct injection [1]. Gasoline direct injection (GDI) engines inject fuel directly into the combustion chamber, offering several appealing features. This approach allows sophisticated control of the injection process, including multiple injections and high-pressure injection, regardless of intake valve timing or manifold geometry [2,3]. From a thermodynamic perspective, direct injection allows higher engine volumetric efficiencies than conventional port fuel injection (PFI) engines because the fuel vapor does not occupy any volume in the incoming charge, allowing for additional air to enter the cylinder during the intake stroke. Moreover, direct injection mitigates knocking by utilizing evaporative cooling enabled by the phase change of the injected liquid fuel, which effectively reduces the in-cylinder temperature [4]. The current state-of-the-art GDI engines demonstrate synergetic effects with additional modification by introducing water injection, pre-chamber, and flexible fuel utilization to further reduce knocking tendency and engine performance [5–8]. Additionally, the injection of fuel, along with swirl and tumble motion, can create a highly turbulent charge motion, which facilitates air-fuel mixing and flame propagation [9,10]. Since the spray process plays an important role in GDI engines, precise spray control throughout all stages of the engine's operating

---

Nomenclature

C_{ext}	extinction coefficient [mm^2]
d	droplet diameter [mm]
I	transmitted light intensity [a.u.]
Re	Reynolds number
V	mean injection flow velocity [m/s]
μ	dynamic viscosity [Pa s]
P	pressure difference across the nozzle [Pa]
PLV	projected liquid volume [mm^3(liquid)/mm^2]
τ	optical thickness [a.u.]
I_0	incident light intensity [a.u.]
ρ_{fuel}	fuel density [kg/m^3]
d_o	nozzle hole diameter [mm]
ν	kinematic viscosity [m^2/s]

Abbreviation

aSOI	After start of injection
CAD	Crank angle degree
CO	Carbon monoxide
CT	Computed tomography
EOI	End of injection
GDI	Gasoline direct injection
HC	Hydrocarbon
LED	Light emitting diode
LVF	Liquid volume fraction
PDA	Phase Doppler anemometry
PM	Particulate matter
SMD	Sauter mean diameter
CFD	Computed Fluid Dynamics
DBIEI	Diffused backlight illumination extinction imaging
FPS	Frame per second
HOV	Heat of vaporization
LHV	Lower heating value
MON	Motor octane number
PLV	Projected liquid volume
PDI	Particulate matter index
RON	Research octane rating
TTL	Transistor to transistor logic

cycle is crucial. Inappropriate settings in the injection strategy can lead to deterioration in fuel consumption and pollutant emissions, for instance under cold-start conditions when fuel spray suffers from poor air-fuel mixing and can cause wall-wetting and pool fire issues. In cold conditions, overall in-cylinder temperature decreases primarily due to enhanced heat transfer to the colder cylinder head and engine block during the compression stroke [11]. The adverse thermal conditions, combined with the unfavorable change in fuel properties, negatively impact the mixture preparation process during the ignition delay period. As a result, this leads to misfires and emissions of hydrocarbons (HC), carbon monoxide (CO), and particulate matter (PM) due to inadequate air-fuel mixing [12–14]. In diesel engines, this issue can be mitigated with ignition aids such as glow plugs that raise the start of compression air temperature and correspondingly can achieve higher end of compression conditions within the combustion chamber, however, this is not applicable for GDI engines because the glow plug can unintentionally create a hot spot (ignition source) later in the cycle and results in cause auto-ignition and knocking [8,15–17].

Various progresses in non-invasive optical diagnostics have been made to describe spray characteristics under cold-start conditions [18–21]. Aleiferis et al. conducted an experimental study on the spray and combustion characteristics of gasoline and E85 fuels using a multi-hole GDI injector [22]. The investigation was carried out in both a quiescent optical chamber and an optically-accessible engine, with the fuel temperature varying from 20 °C to 120 °C. Multiple techniques such as high-speed Mie-scattering, shadowgraphy, and Phase Doppler Anemometry (PDA) were employed to analyze liquid vapor distribution and droplet sizing, respectively. Under cold-start conditions, individual spray plumes exhibited slower evaporation, resulting in thinner plume cone angles and longer liquid penetration distances. Analysis using non-dimensional parameters, namely Reynolds (Re) and Weber (We) numbers, revealed that these values were halved at 20 °C compared to 120 °C fuel temperature. Consequently, larger droplet sizes of about 10 μm were observed under cold conditions. The deterioration in the spray and air-fuel mixing process resulted in delayed combustion phasing. The peak in-cylinder pressure was reduced by 25 %, and the timing was delayed by 10 crank angle degrees (CAD) with 20 °C fuel temperature compared to 120 °C. Direct flame imaging confirmed a decrease in the global flame centroid speed from 12 m/s to 7 m/s as the fuel temperature decreased. Regarding the test fuels, the spray process of E85 was found to be less sensitive to changes in fuel temperature compared to gasoline. E85 spray plumes exhibited a thinner and more compact

structure at low temperatures, resulting in higher spray penetration. Meanwhile, Huang et al. conducted a similar experimental investigation using an asymmetric GDI injector and shadowgraphy imaging in a constant volume chamber [23]. They examined the effects of gasoline and ethanol fuel temperature variations ranging from 0 °C to 120 °C. The experimental results indicated that the start of injection occurred earlier under high fuel temperature conditions. This observation is consistent with previous research suggesting that the movement of the solenoid needle, which controls injection timing, is influenced by fuel viscosity [24]. Additionally, an analysis of spray breakup using the Weber number (We) demonstrated that within the temperature range of 0 °C to 230 °C, the ethanol spray underwent all three breakup mechanisms: bag breakup (We > 80), stripping breakup (80 < We < 350), and catastrophic breakup (We > 350). In contrast, the gasoline spray experienced only bag breakup and stripping breakup regimes. In addition to experimental observations, Computational Fluid Dynamics (CFD) simulations have demonstrated considerable potential in guiding optimization efforts for cold-start conditions. A recent study by Jing et al. employed CONVERGE software to simulate the behavior of cold GDI sprays [25]. The study validated spray parameters such as liquid penetration and Sauter mean diameter (SMD) using experimental data obtained from constant chamber experiments. Subsequently, engine simulations were performed. Consistent with the experimental findings discussed earlier, the CFD simulations also revealed longer penetration lengths and reduced fuel evaporation under 20 °C compared to the 80 °C fuel temperature case. Consequently, a significant amount of liquid fuel, 4.2 mg out of total 12 mg injection mass, was impinged on the piston top and cylinder wall with cold fuel, which was notably higher than the 1.3 mg observed in the hot fuel case. The simulations also highlighted non-homogeneity in the air-fuel mixture at lower fuel temperatures, which can contribute to higher cycle-to-cycle variation during cold-start conditions.

Despite previous efforts, current imaging approaches for studying cold-start GDI sprays, such as Mie-scattering and Schlieren imaging, are limited to line-of-sight 2D measurements. These methods provide qualitative data rather than detailed quantitative information, making them insufficient for validating CFD simulations. To address this limitation, this study employs three-dimensional computed tomography (3D CT) techniques to gain detailed insights into the plume dynamics of cold-start GDI sprays. By capturing projected liquid volume (PLV) measurements from three viewing angles, we acquired three-dimensional information on the liquid volume fraction (LVF). This novel diagnostic

method offers several advantages, including cost-effectiveness, reduced measurement time, and improved spatio-temporal resolution. It not only provides a comprehensive understanding of plume dynamics but also enables quantitative validation of local LVF across the entire spray domain. The primary objective of this study is to investigate the comprehensive spray process of cold-start GDI sprays using a combination of measurement techniques, including line-of-sight PLV measurement, 3D CT, Schlieren, and microscopic imaging. A series of optical imaging were conducted in a constant volume spray vessel, utilizing a gasoline surrogate fuel known as PACE-20 [26]. The analysis of the high-speed imaging results focused on macroscopic spray characterization as well as microscopic features of liquid ligament dynamics and droplet sizing. These detailed measurements of cold-start spray characteristics using PACE-20 will provide quantitative data that can be valuable for directly validating future CFD simulations.

Test procedure and condition

Test injector and fuels

A GDI injector (THN216, KEFICO) with eight axisymmetric nozzles was utilized for spray test. To obtain detailed geometry for future CFD purposes, the test injector was scanned using a commercial x-ray scanner (XT H225, Nikon), as shown in Fig. 1. Each nozzle, drilled at an angle of 26.6°, had an inner orifice and counter-bore diameter measurements of 150.6 μm and 360.4 μm, respectively. For spray initiation, a 5 V TTL signal was sent to the injector driver, as well as to a high-speed camera to trigger recording. Conditioned coolant was circulated in a cooling/heating jacket around the injector for 12 h to ensure consistency in the experiment and a 1/16 in thermocouple was installed near the tip of the injector shown in Fig. 1(c) to measure the injector temperature and approximate the fuel temperature. The minimum temperature in the circulator tank that could be achieved was −20 °C; however, the lowest injector tip temperature achieved was −7 °C due to heat transfer to the vessel and coolant lines. The fuel injection pressure was controlled using a syringe pump (Syrixus 65x, Teledyne ISCO). During the experiment, injection pressure, fuel and ambient temperature were controlled in a range of ±1 bar, ±0.5 °C, and ±1 °C, respectively.

As test fuel, a multi-component surrogate fuel called PACE-20 was used. PACE-20 fuel was developed to capture the realistic evaporative spray characteristics of gasoline. This was a part of the Department of Energy's 'Partnership for Advanced Combustion Engines (PACE), a light-duty national laboratory combustion consortium project representing the US market E10 gasoline [26,27]. The composition and fuel properties of PACE-20 are listed in Table 1, and its distillation characteristics are presented in Fig. 2. It is daunting to perform numerical analysis with commercial gasoline that contains hundreds of different species, but PACE-20 facilitates future CFD simulation thanks to known chemical compositions and similar fuel properties to commercial

Table 1

(a) Composition of PACE20 in liquid volume fraction, and (b) fuel properties compared to regular E10 gasoline.

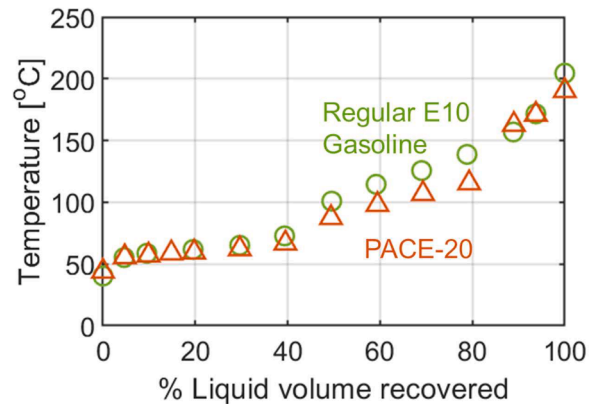| Species	LVF [%]	
N-pentane	0.1395	
N-heptane	0.1153	
Iso-octane	0.2505	
Cyclo-pentane	0.1050	
Toluene	0.0919	
1,2,4-Trimethylbenzene	0.1187	
Tetralin	0.0295	
1-Hexene	0.0541	
Ethanol	0.0955	
(a)		
Property	PACE20	Regular E10 Gasoline
RON	92.1	92.3
MON	84.5	84.6
H/C ratio	1.964	1.969
Density at 15 °C [g/mL]	0.742	0.750
LHV [MJ/kg]	41.71	41.77
PMI	1.51	1.68
HOV [kJ/kg]	407.5	419.9
(b)		

Fig. 2. ASTM D86 distillation curve of PACE-20 and a research-grade regular E10 gasoline.

gasoline.

High-speed imaging setup

Spray test was carried out within a constant volume vessel under controlled pressure and temperature conditions. The spray vessel testing offers numerous advantages when compared to optical engines: (1) The vessel system enables the separate control of thermodynamic factors. By
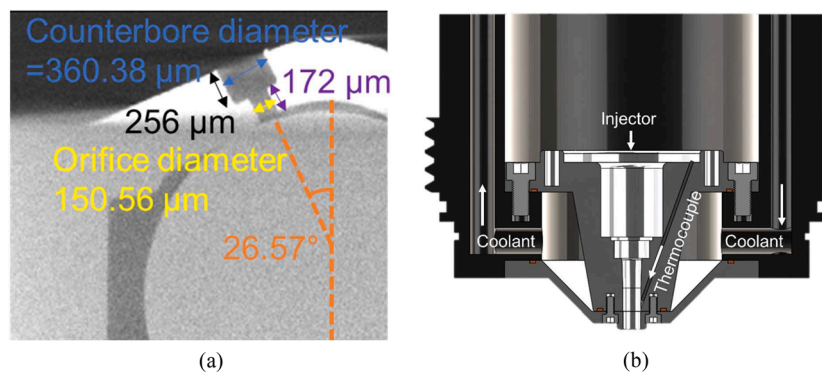

Fig. 1. (a) X-ray scanned image showing plume direction angle of 26.6°, inner orifice diameter of 150.6 μm, and counterbore diameter of 360.4 μm, and (b) cut plane view of injector adaptor, 1/16 in thermocouple was installed to measure injector tip temperature.

analyzing the spray process under defined boundary conditions, a profound comprehension of how each thermodynamic parameter affects spray characteristics is promoted. (2) The vessel system provides extensive optical access, surpassing that of an optical engine where visibility is confined to portions of the piston or cylinder liner. This expanded access facilitates simultaneous imaging from various angles and supports multiple diagnostic techniques. (3) Unlike optical engines, the spray vessel minimizes liquid impingement on surfaces and enables full visualization of spray process in time. Optical engines often experience issues with spray causing wetting on cylinder walls or pistons depending on ambient conditions. On the contrary, the constant spray vessel's volume prevents wall impingement, allowing the complete spray process to be captured without obstruction. In essence, the primary objective behind compiling the spray vessel dataset is to offer dependable experimental data with precisely controlled boundary conditions. This dataset serves as a trustworthy validation resource for modeling endeavors.

Spray vessel used for the testing has five ports, including one specifically designed for the injector, and two parallel windows dedicated to high-speed extinction (liquid) and Schlieren (vapor) imaging. Quartz windows, with a diameter of 90 mm, were installed in the ports to enable visualization of the spray region within the vessel. Fig. 3 illustrates the experimental setup for simultaneous extinction and Schlieren imaging.

This study uses the Diffused Backlight Illumination Extinction Imaging (DBIEI) technique to examine the liquid phase of the injected fuel. This setup uses a high-speed green LED in conjunction with a Fresnel lens (150 mm, f = 150 mm), an engineered diffuser, and a band-pass filter (center wavelength: 527 nm, bandwidth: 20 nm, full width at half max: 22 nm). The imaging process employed a high-speed digital video camera (Phantom, v611) equipped with a prime lens (AF Nikkor 50 mm f/1.8D, Nikon) to capture the development of the spray inside the vessel. The green LED was activated with a 60 ns TTL command signal duration to capture the spray within the visualized frame. The camera was configured with a shutter speed of 14,000 frames per second (fps) and an image resolution of 608 by 608 pixels. The lens aperture was set to 2.8, and the camera's exposure time was 38 μs. An engineered diffuser (20°) was used to ensure a consistent light field and mitigate beam steering caused by evaporation and temperature fluctuations. The DBIEI technique specifically focused on capturing extinction signals from the liquid phase of the fuel and was able to exclude the vapor phase. The injector was positioned in the chamber using a rotating adaptor, allowing precise angle alignment for orientation clocking while maintaining a secure chamber seal and consistent fuel supply pressure. This setup enabled the variation of the viewing angle of the spray while keeping the camera positions fixed, facilitating the acquisition of PLV images at different viewing angles for 3D computed tomography (CT) reconstruction. DBIEI was conducted at three different viewing angles of

0°, 11.25°, and 22.5° from the initial clocking orientation. For each position of the injector, a total of 20 injections were recorded. The injector rotation followed a clockwise direction when observing the nozzle tip. Prior to each set of recordings, background (dark) frames were captured without any lighting, and the initial intensity was measured for 10 frames before injection to establish a reference illumination intensity for each pixel. This process was carried out within the camera's appropriate count range to ensure accurate measurement of the extinction signal without encountering zero or saturated pixels.

To visualize the vapor fuel distribution along a line of sight, Schlieren imaging was performed using a z-type Schlieren configuration. Same model of high-speed camera employed for extinction imaging was used, along with a prime lens (AF-S Nikkor 85 mm f/1.8G, Nikon). To generate an effective point source, light from a red LED with a duration of 500 ns was collected and focused through a lens (Nikkor, 50 mm f/1.8), passing through a 0.5 mm diameter aperture. The resulting expanding light was collimated using a concave mirror (GSO, 152 mm f/6.0), and the parallel light rays were directed through the spray region. After traversing the spray, the parallel light was collected by an identical concave mirror, and a knife-edge with approximately 50 % cut-off was positioned at the focal point to enhance sensitivity. The imaging setup for Schlieren was the same as the one used for extinction imaging, consisting of the camera and LED arrangement.

Finally, microscopic imaging was conducted to capture subtle features of the fuel sprays in the near field of the fuel injector. For this purpose, an identical high-speed camera and extinction setup were utilized, along with a long-distance microscopic lens (Infinity DistaMax - K2 lens). The camera resolution was set to 512 by 512 pixels, resulting in a pixel scale of 3.8 μm/pixel. At this resolution, the camera achieved a frame rate of 21,000 fps. The same LED and band-pass filter components used for extinction imaging were also employed for microscopy. During each injection cycle, a total of 300 frames (~14 ms) were recorded to gather information on droplet sizes after the termination of the injection event (which lasted for approximately 1.5 ms). A total of 20 injections were recorded to ensure reliable and statistically significant measurement quantities and derived averaged values, standard deviation, and droplet-size distributions.

Image processing method

Projected liquid volume (PLV) measurements

Extinction imaging is advantageous for spray characterization because it provides more quantitative information on liquid fuel concentration compared to conventional Mie-scattering imaging. Mie-scattering imaging encounters uncertainties related to illumination and scattering processes; thus, extinction imaging is becoming a standard diagnostics in the spray research community [28]. This study
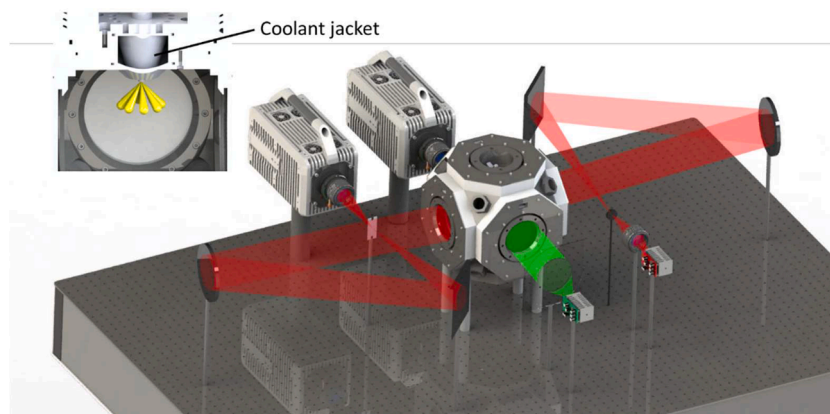

Fig. 3. Mississippi State University's constant volume spray vessel with simultaneous high-speed extinction and Schlieren imaging setup. Green and red LEDs were utilized for extinction and Schlieren, respectively.

followed same procedure of raw image conversion process into PLV that published in our previous work [29]. In extinction imaging, the measured optical thickness, droplet size, and extinction coefficient are utilized to derive the PLV along a line of sight. This PLV can be directly compared with CFD results. The optical thickness in a spray region can be calculated using the Beer–Lambert law, which is expressed as follows.

$$\tau = -\ln(I / I_o) \tag{1}$$

In the Beer–Lambert law, the transmitted attenuated light intensity, denoted as *I*, is influenced by the interaction with the liquid spray. I_o represents the incident light intensity in the absence of any extinction (background image). The extinction is primarily caused by scattering off the liquid fuel droplets, resulting in measurable attenuation within the camera's dynamic range. On the other hand, the contribution of vaporized fuel to extinction is negligible. However, gradients in fuel vapor concentration and temperature can lead to beam steering effects, which can be mitigated by employing engineered diffusers [30]. These diffusers help to reduce the impact of beam steering and ensure more accurate liquid measurements. The measured optical thickness, denoted as τ, is directly related to the PLV. The PLV represents the integral of the liquid volume fraction (LVF) along the cross-stream direction y, and the correlation between τ and PLV is given by the following equation.

$$PLV = \tau \frac{\pi d^3/6}{C_{ext}} = \int_{-y_\infty}^{y_\infty} (LVF) \cdot dy \tag{2}$$

Eq. (2) incorporates Mie-scattering and extinction theories, assuming that the droplet diameter (*d*) and extinction coefficient (C_{ext}) remain constant along the line of sight. The PLV indicates the amount of liquid volume within a specific projected area and is measured in units of $mm^3(liquid)/mm^2$. To derive PLV quantitatively, it is crucial to determine the values of important parameters such as droplet diameter (*d*) and extinction coefficient (C_{ext}). The extinction coefficient was calculated based on the optical setup using MiePlot program [31]. This study assumed a constant droplet diameter of 12 μm throughout the injection event. The refractive index of the fuel was assumed to be 1.35.

Fig. 4 illustrates PLV conversion from the raw image. Firstly, a specific frame from an individual injection event is selected and corrected for the dark signal by subtracting the averaged dark frame (floating intensity in the camera sensor). Subsequently, the spray image is divided by the appropriately scaled illumination image from the same injection event, considering the pulse-to-pulse variation in LED brightness. This scaling is achieved by examining two regions in the field of view that are far from the spray and experience no extinction. The entire frame correction process is performed for each of the 300 frames captured during an individual injection event. Then, the corresponding frames from each of the 20 sequentially recorded injection events are ensemble-averaged to minimize the influence of random variations in the spray. The resulting averaged and corrected optical thickness values are then converted into PLV values using Eq. (2). In this study, the threshold value of $0.2 \cdot 10^{-3}\,mm^3(liquid)/mm^2$ was applied to process and binarize PLV images (spray outline) according to this threshold value. In the binarized image, liquid penetration length was defined as the farthest axial distance from the nozzle at the primary viewpoint (0° rotation angle) and the spray liquid width was measured at axial distances of 15 mm and 30 mm away from the nozzle tip. These locations are standard criteria for CFD validation in Engine Combustion Network (ECN) community [32], and they can show transient plume dynamics in line-of-sight measurements.

3D computed tomography

As described in Section 2.2, the PLV data obtained from three different viewing angles were transformed into 3D spray LVF data using a CT algorithm. To accomplish this, a sinogram was constructed by stacking the extracted z-plane PLV profiles from each viewing angle. The reconstruction process was conducted using MATLAB's built-in "iradon" function, that utilizes the filtered back-projection algorithm for performing the inverse Radon transform. The reconstruction was applied to axial planes spanning from the nozzle tip to $z = 60$ mm downstream. A Hamming filter parameter of 0.3 was employed during the reconstruction process. Detailed procedures for accomplishing the 3D CT utilized in this study have been previously disclosed by Weiss et al. [33] and Hwang et al. [29].

Schlieren intermittency

The Schlieren image processing routine is presented in In Fig. 5. First, the initial background intensity I_o was subtracted from the spray image *I* to isolate the spray region (Fig. 5(a)). The vapor envelope was then identified using MATLAB's built-in "imgradient" function, which calculates the spatial gradient magnitude, as depicted in Fig. 5(b). This gradient magnitude image was binarized using a specific threshold value, as shown in Fig. 5(c). Subsequently, the area inside the vapor boundary (where the gradient magnitude is low due to the presence of liquid spray) was filled to create a connected vapor boundary. This step was achieved using MATLAB's built-in "bwperim" function, and the resulting boundary was visualized. This allows visual verification of the image processing routine. The vapor penetration length was defined at each injection and time step as the distance between the nozzle tip and the farthest axial point on the vapor boundary. Additionally, a vapor probability map was generated by summing the binarized images, as illustrated in Fig. 5(d). This summation provided an indicated vapor intermittency based on the presence or absence of vapor in the recorded images across 20 injections.

Droplet sizing

The microscopic images were carefully examined to extract the distribution of droplet sizes at the conclusion of the injection process. This analysis is crucial for comprehending spray atomization, fuel/air
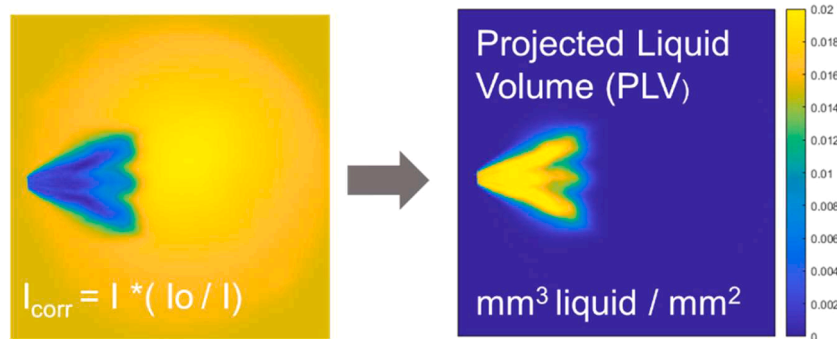

Fig. 4. Procedure to acquire projected liquid (PLV) map from raw extinction image left shows optical thickness from 20 averaged extinction images, and right indicates converted PLV through Eq. (2).
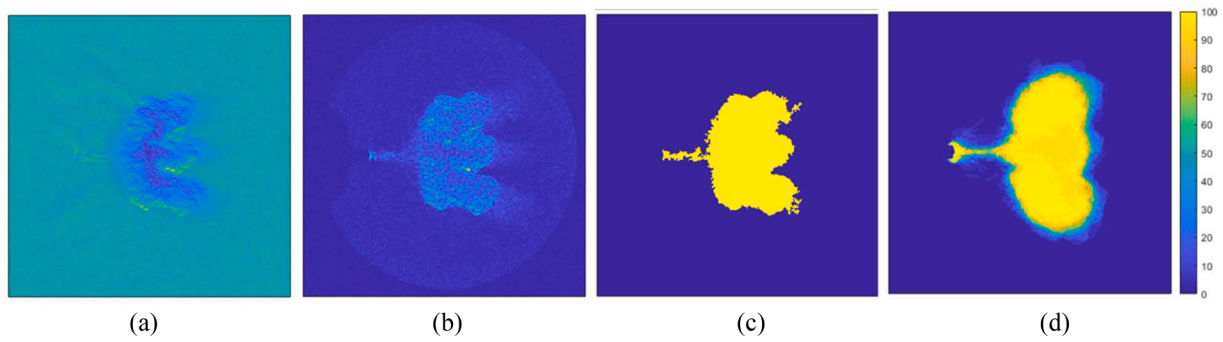
Fig. 5. Image processing routine for Schlieren image (a) raw image, (b) gradient image, (c) binarized image, and (d) vapor intermittency.

mixing, and the formation of soot due to fuel dribbling [34]. The process of automatically identifying the probability distribution function of droplet size involved several steps, as depicted in Fig. 6.

Image processing starts with a background image that is at an initial frame of each image sequence captured before the spray injection. Based on this background image, a mask (Fig. 6(a)) was created to blank out the region occupied by the injector. Starting from the end of injection (EOI), each subsequent image frame (Fig. 6(b)) was subtracted from the background image to calculate the difference in light intensity. The resulting difference image was rescaled (Fig. 6(c)). In order to identify only the in-focus features, the gradient was calculated. The gradient magnitude was then masked and binarized. Closed curves of the binary regions were filled, and small features (below 3 pixels, equivalent to a droplet diameter of ~10 µm) as well as large ligaments (greater than 12 pixels, equivalent to a droplet diameter of ~45 µm) were filtered out. The resulting binarized gradient image (Fig. 8(d)) of each frame served as input to MATLAB's built-in "regionprops" function, which identified

the center and size of the circles corresponding to the binarized images (Fig. 6(e)). The diameters of all the identified features were recorded for each frame across all injection cycles. After collecting all the statistical data, a histogram of the droplet sizes (Fig. 6(f)) was derived based on the data from 20 injections. It is important to note that this procedure is primarily applicable to larger droplets and may have limitations in accuracy for droplets that are slightly out of focus due to the circle of confusion. However, this approach is still useful for detecting trends associated with different fuel temperatures.

Test conditions

The spray experiments were conducted under cold-start early injection conditions. The ambient temperature was set to 20 °C, and the pressure was set to 1 bar that is corresponding to early injection case in engines. The temperature of the injector tip varied in five levels from −7 °C to 60 °C using a coolant circulator. The injection pressure was
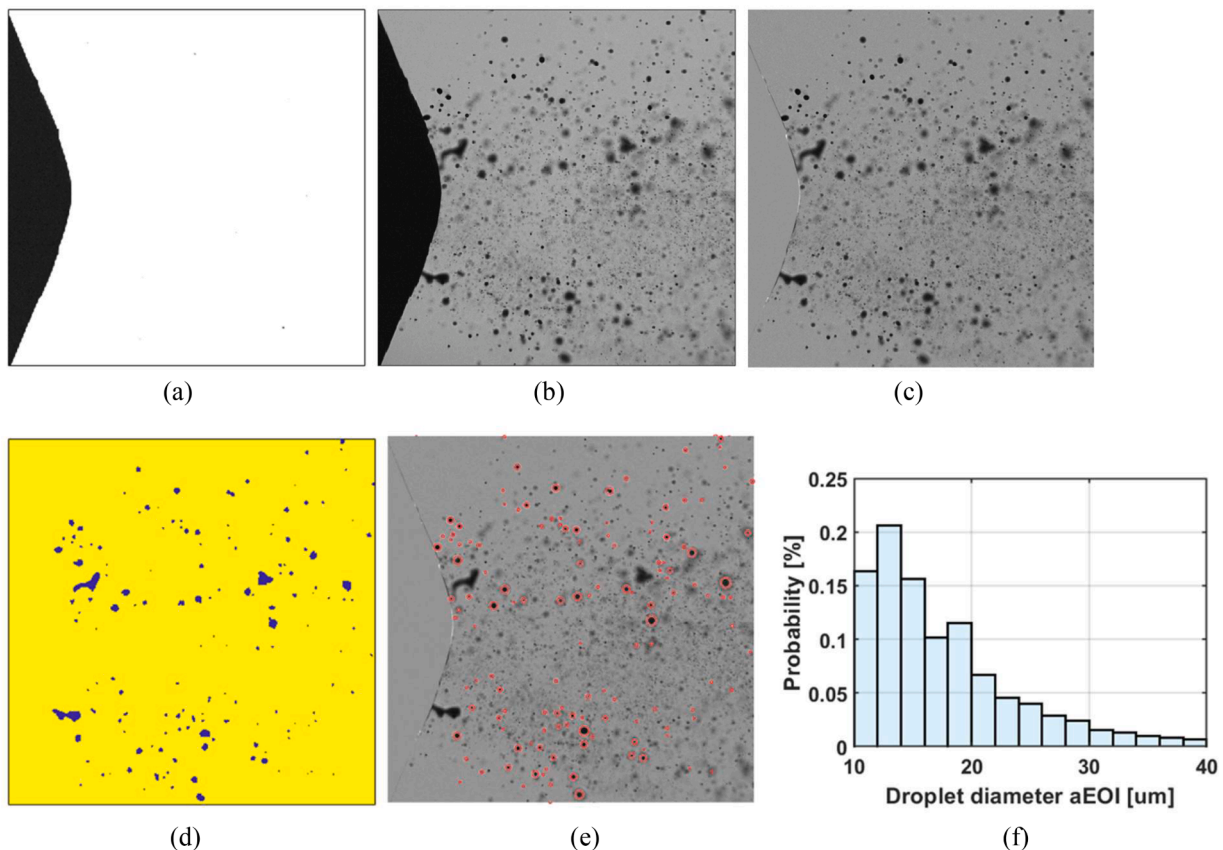

Fig. 6. Droplet sizing identification process.

adjusted in seven levels in the range of 50 bar to 350 bar. The electronic injection duration was kept constant at 1.5 ms throughout the experiments to minimize aerodynamic driven flow effects on plume dynamics, but to ensure maximum needle lift regardless of injection pressures. These conditions allowed for investigating the spray behavior and characteristics under specific temperature and pressure conditions relevant to cold-start engine operation.

Results and discussion

Line-of-sight liquid and vapor spray

Fig. 7 presents the results for PLV Fig. 7(a)) and Schlieren intermittency (Fig. 7(b)), for a single injection pressure of P_{inj} = 50 bar at two different fuel temperature conditions of −7 °C and 60 °C as well as liquid/vapor length and liquid width (Fig. 7(c)) for three different injection pressure conditions of P_{inj} = [50, 150, 350] bar and T_{fuel} = [−7, 20, 60] °C. The liquid penetration was measured with a $0.2 \cdot 10^{-3}$ mm³(liquid)/mm² threshold. The mean standard errors ($\pm 2\sigma/\sqrt{n}$) of liquid penetration and width were too small to be present in the figure. It should be noted that the results are synchronized with the timing after actual start of injection. However, in the raw images, there was an injection delay detected, which is the time interval between the start of the electronic command and the actual hydraulic flow under cold fuel conditions. Consequently, the initial spray development for the cold fuel was slower compared to hot fuel cases. This behavior is attributed to the fuel property, especially increased fuel viscosity as the temperature decreases [35]. It is reported that kinematic viscosity is 30 % higher at −10 °C than 40 °C fuel temperature condition [36]. This causes higher friction between the injector needle and the fuel, so the needle opening and closing events are physically slower. Similarly, our microscopic imaging in Section 3.3 will show the later closing of the needle at cold fuel conditions. In the present experimental conditions, where the injector configuration, injection signal, and injection pressure were kept identical, the shear stress (expressed in Eq. ((3), μ dynamic viscosity, u is liquid velocity and y is distance) with fuel at −7 °C is approximately doubled in comparison to that of the fuel at 60 °C due to its higher viscosity. This finding is consistent with previous studies that cold fuel reduced the flow performance of a solenoid type injector [24,37].

$$\tau_{shear} = \mu \left(\frac{\delta u}{\delta y} \right) \tag{3}$$

Despite the slower spray development observed at −7 °C fuel temperature, the liquid penetration was greater at the injection pressure of 50 bar condition. The raw images showed the presence of ballistic droplets that were not fully atomized at the leading edge in the low fuel temperature cases. On the other hand, as the injection pressure increased, an opposite trend was captured that the liquid/vapor penetration became longer with hot fuel conditions. The liquid/vapor penetration at 60 °C gradually got longer than the −7 °C case as injection pressure increased. There was also a larger difference in liquid width between the distances of 15 mm and 30 mm at the high fuel injection pressure case. In the PLV and Schlieren intermittency images, the spray morphology at 60 °C exhibited a strong plume collapsing toward the spray core area, resulting in accelerated liquid/vapor penetration in the axial direction due to the spray momentum. This process will be further investigated in the next section using 3D spray analysis. Another notable difference depending on the fuel temperature is that, even though the hot fuel exhibited plume movement towards the center, which restricts air entrainment into the spray, the level of PLV decreased faster compared to the cold fuel.

3D Liquid volume fraction (LVF) comparison

In Fig. 8, the three-dimensional LVF (liquid volume fraction) data is presented, showing the spatio-temporal distribution of the spray. The data reveals the phenomenon of plume collapsing, which is characterized by strong plume movement towards the core area of the spray. This effect becomes more pronounced with higher injection pressure and fuel temperature.

To gain further insight into the plume dynamics, a cut plane view at the center plane is presented in Fig. 9. In the cut plane liquid boundary plot, the dotted line indicates the nozzle drill angle of 26.6° from the injector axis. The liquid boundary was determined using an LVF threshold of $0.3 \cdot 10^{-4}$. It is important to note that this specific value corresponds to LVF and should not be mistaken for the projected criteria of $0.2 \cdot 10^{-3}$ mm³ (liquid)/mm² used for PLV in the previous section. The LVF value obtained through the plume center represents an average obtained from 8 plumes. The liquid contour observed at the center plane provides detailed information about the plume dynamics, including the movement of the plumes toward the center, as well as individual plume direction angles and thickness.

In the contour graph, it is confirmed that individual plume thickness got smaller as fuel temperature decreased. This can be analyzed with non-dimensional number, Reynolds number (Re) that assesses the atomization characteristics of the fuel spray. The Reynolds number represents the ratio of inertia to viscosity and can provide insights into the flow behavior.

$$Re = \left(\rho_{fuel} V d_o \right) / \mu = (V d_o) / \nu \tag{eq-3}$$

$$V = \sqrt{\frac{2\Delta P}{\rho_{fuel}}} \tag{eq-4}$$

The turbulent intensity within the internal nozzle flow increases with the Re, where it is determined by factors such as fuel density (ρ_{fuel}), mean injection flow velocity (V), nozzle hole diameter (d_o), dynamic viscosity (μ), kinematic viscosity (ν), and the pressure difference across the nozzle (P). This turbulence plays a role in promoting boundary layer separation and spray diffusion along the radial direction. The Re numbers were calculated to be 19,703, 23,847, and 25,112 for temperatures of −7 °C, 20 °C and 60 °C, respectively, at an injection pressure of 50 bar. The Re number for the cold fuel was approximately 17 % smaller than that of the hot fuel due to its higher viscosity. Consequently, the spray angle of the cold fuel was narrower compared to diesel fuel, indicating a more stable spray structure. Meanwhile, regarding injection pressure, the Re numbers were increased to 2.6 times at 350 bar condition than that of 50 bar injection pressure condition. This indicates that each individual plumes spread more in radial direction (thicker plumes) due to higher momentum exchange between air and fuel spray but finally induces plume-to-plume interaction and the plume collapsing, as shown in the cut plane liquid boundary [38].

Fig. 10 summarizes the plume direction angle as a function of fuel temperature and injection pressure. The values presented are averaged over the first 1 ms of the injection process. The results clearly indicate that as the fuel temperature and injection pressure increase, the plume direction angle becomes smaller, suggesting a collapse of the plume and a potential for liquid fuel impingement on the surface of the piston top and cylinder wall. Considering the original nozzle drill angle of 26.6°, a significant plume collapsing of up to 16° was seen.

In practical engine applications, it is advisable to use a moderate injection pressure, such as below 150 bar, and employ multiple injections to restrict liquid penetration [39]. This approach ensures better air-fuel mixing by enhancing fuel atomization to a certain level and preventing plume collapse, thus minimizing the occurrence of liquid pool combustion on the piston top and cylinder wall [40]. Additionally, an injector with wider nozzle spacing can be employed to improve cold startability, as it facilitates better fuel distribution and atomization during engine startup.
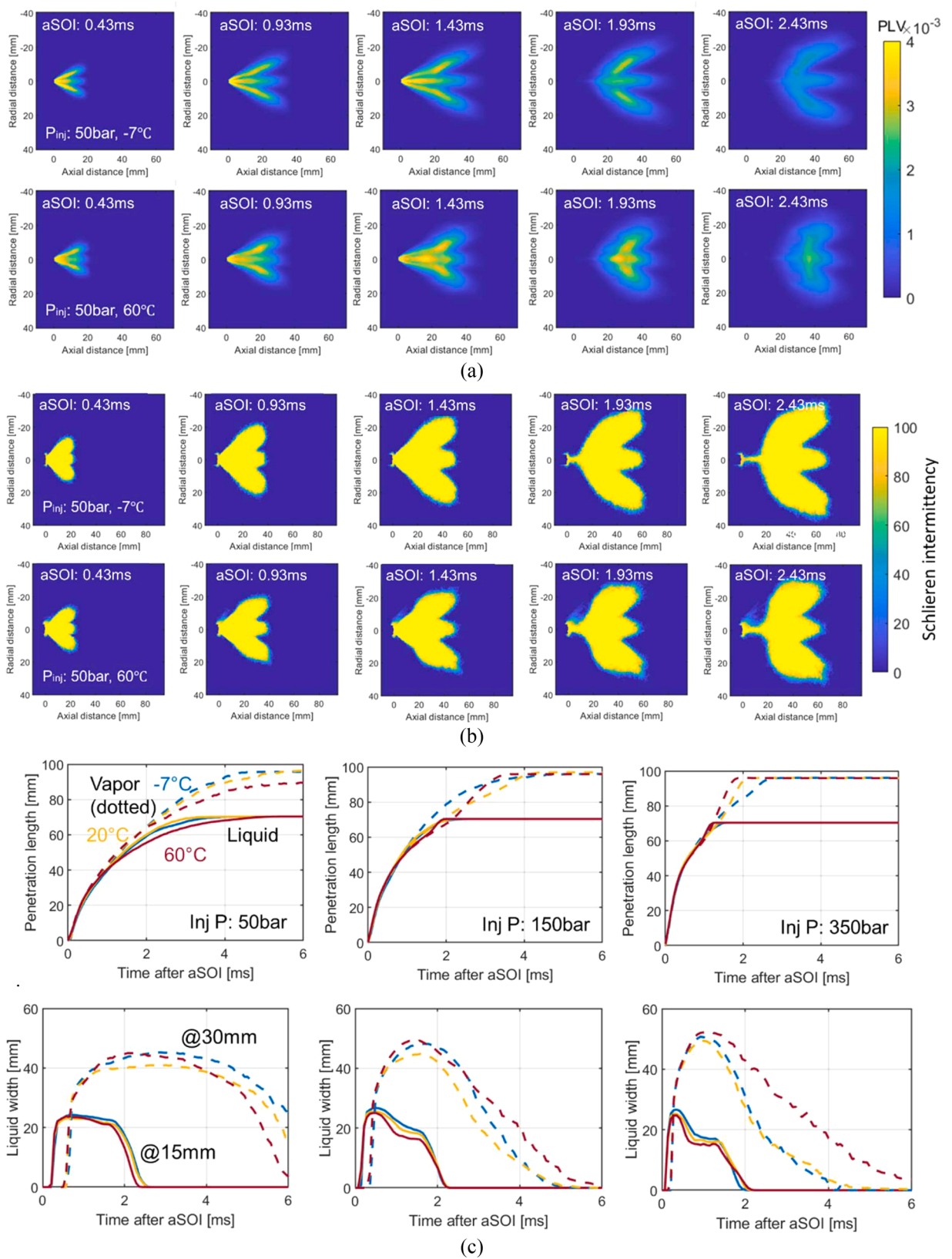
Fig. 7. (a) Averaged PLV from 20 different injections, (b) Schlieren intermittency at top −7 °C and bottom 60 °C fuel temperature, (c) liquid/vapor penetration length with PLV threshold of 0.2·10⁻³ (top), and liquid width (bottom).
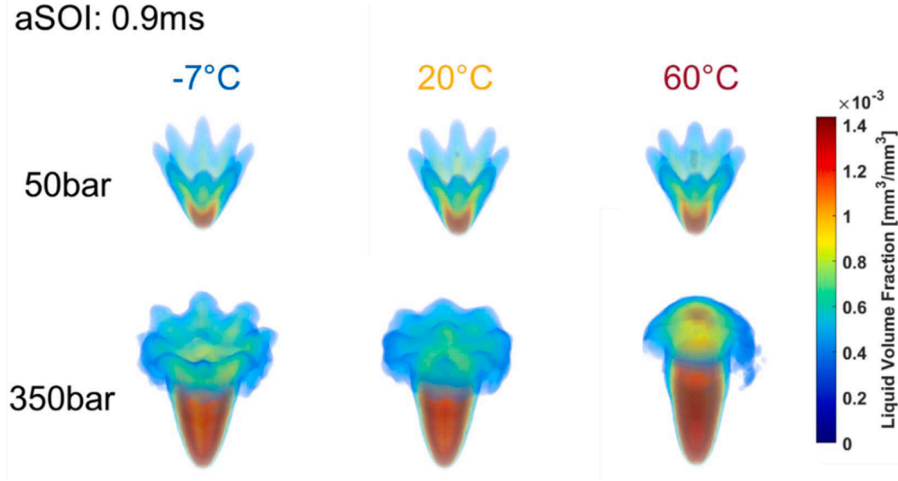
Fig. 8. Three-dimensional liquid volume fraction at 0.9 ms aSOI according to different fuel temperature and injection pressure conditions.
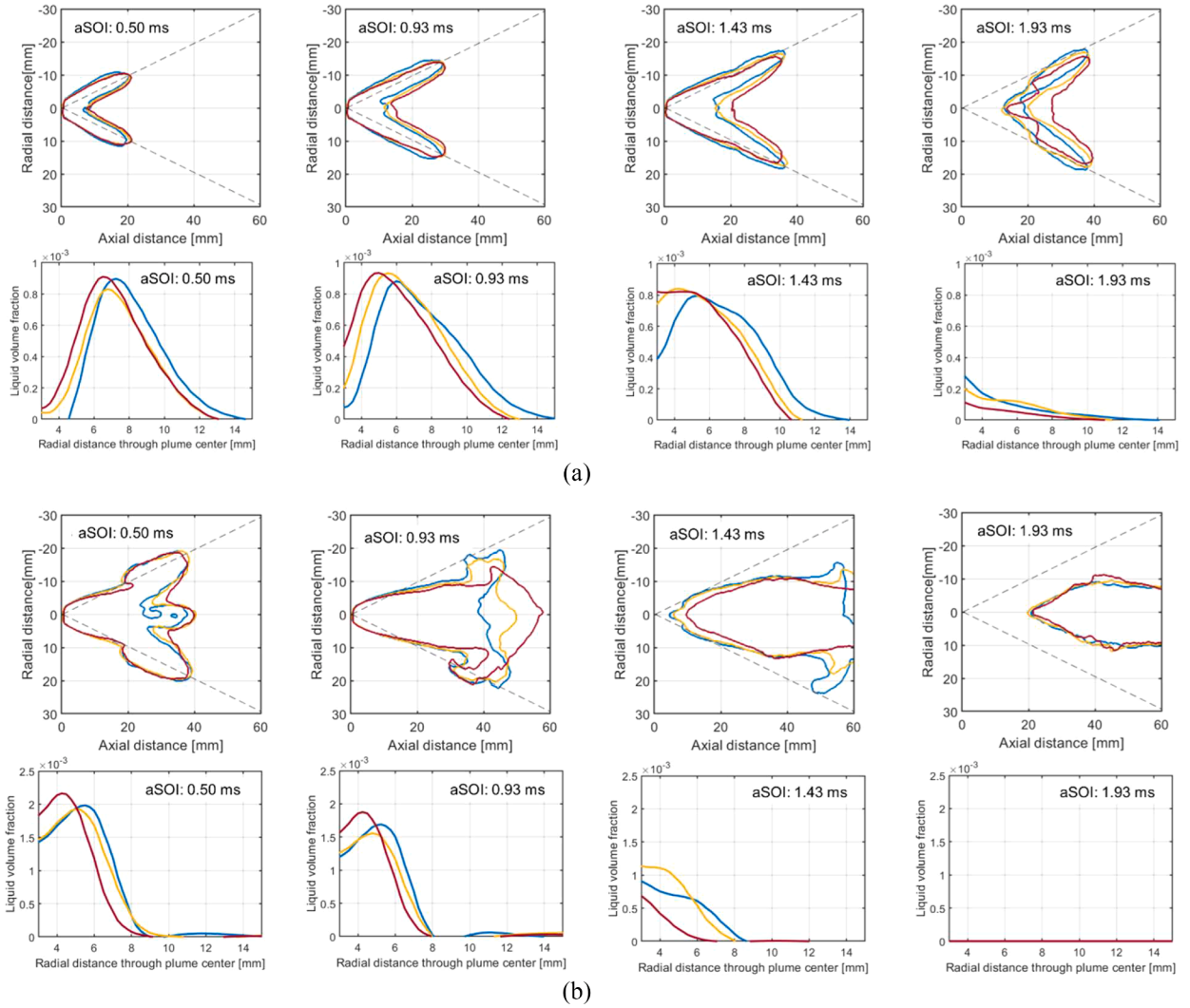

Fig. 9. Liquid spray boundary at center plane with a liquid volume fraction threshold of $0.3 \cdot 10^{-4}$ for (a) 50 bar, and (b) 350 bar injection pressures.

Microscopic spray

In addition to macroscopic spray imaging, supplementary experiments focusing on the near-nozzle region were conducted. Microscopic imaging of the near-nozzle spray, extending downstream by 30 mm, was performed using a backlighting setup. Fig. 11 presents sequential images capturing the near-nozzle spray behavior. During the end-of-injection period, a close examination shows connected liquid ligaments
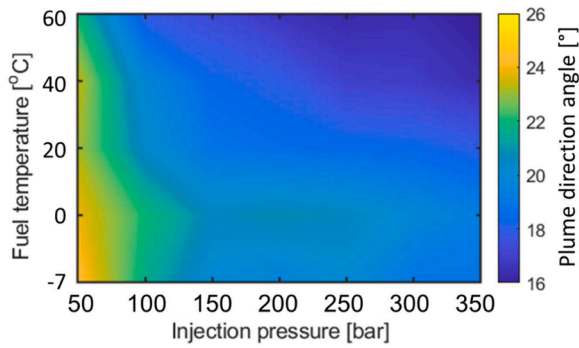
Fig. 10. A contour of averaged plume direction angle during the first 1 ms of the injection period according to fuel temperature and injection pressure conditions.

typically associated with fuel dribbling, but there is greater light extinction for cold condition for a longer period after end of injection suggesting poor atomization and greater time for vaporization.

Meanwhile, under high fuel temperatures, the sprays exhibited intense plume-to-plume interaction right from the nozzle outlet, with no distinct separation between individual plumes along the line of sight. The presence of droplets between plumes hindered the transmission of background light, resulting in reduced background light intensity. During the end-of-injection period, a closer examination revealed that the cold fuel exhibited a longer duration, indicating a delayed needle closing. Furthermore, the cold fuel displayed more connected liquid ligaments, and a greater extent of light extinction was observed after the end of injection, implying an increased vaporization time. A detailed analysis of droplet sizing can be found in the subsequent section.

Quantifying spray behavior during the injection process is challenging due to the high optical thickness and the presence of high turbulence. However, droplet size measurements can be conducted after the end of injection (EOI) when the spray has significantly lost its momentum [41]. Although this characterization provides a general trend rather than an exact size during the injection, it still holds meaningful

information. Fig. 12 presents the probability histogram of droplet size after the EOI (aEOI). Droplets with sizes below 10 μm (3 pixels) were excluded from the analysis to account for the image resolution limitations. The probability histogram was derived from 20 injections. The results of droplet size clearly demonstrate differences based on the fuel temperature. There was little difference in droplet size distribution according to fuel temperature. The average droplet diameter for the cold fuel temperature was approximately 1 μm larger than that for the hot fuel temperature. This is not a notable difference according to fuel temperature; however, droplet temperature also affects evaporation so cold fuel spray results in slower mixture formation.

Conclusion

This study examined the effects of fuel temperature and injection pressure on spray morphology using practical gasoline direct injection injectors under simulated cold-start conditions in a constant volume18 vessel. A series of spray tests were conducted, and the liquid/vapor morphology as well as plume dynamics were characterized using innovative spray characterization techniques such as LED-based diffusive back-illuminated extinction imaging, Schlieren imaging, and 3D computed tomographic image reconstruction. The experimental results revealed several key findings regarding the influence of fuel temperature and injection pressure on spray morphology as follows.

- The actual start and end of fuel injection were delayed as the fuel temperature decreased. This delay was primarily attributed to the higher viscosity of the cold fuel, which exerted greater shear force on the needle and restricted its movement. Although the penetration development was slower, the cold fuel exhibited a longer penetration length and narrower plume width compared to hot fuel conditions. This can be attributed to reduced fuel evaporation and diminished air entrainment into the plume.
- Detailed analysis using 3D computed tomography imaging elucidated that the cold fuel had narrower individual plume angles, resulting in lower plume-to-plume interaction compared to hot fuel conditions. The differences in spray morphology between cold and
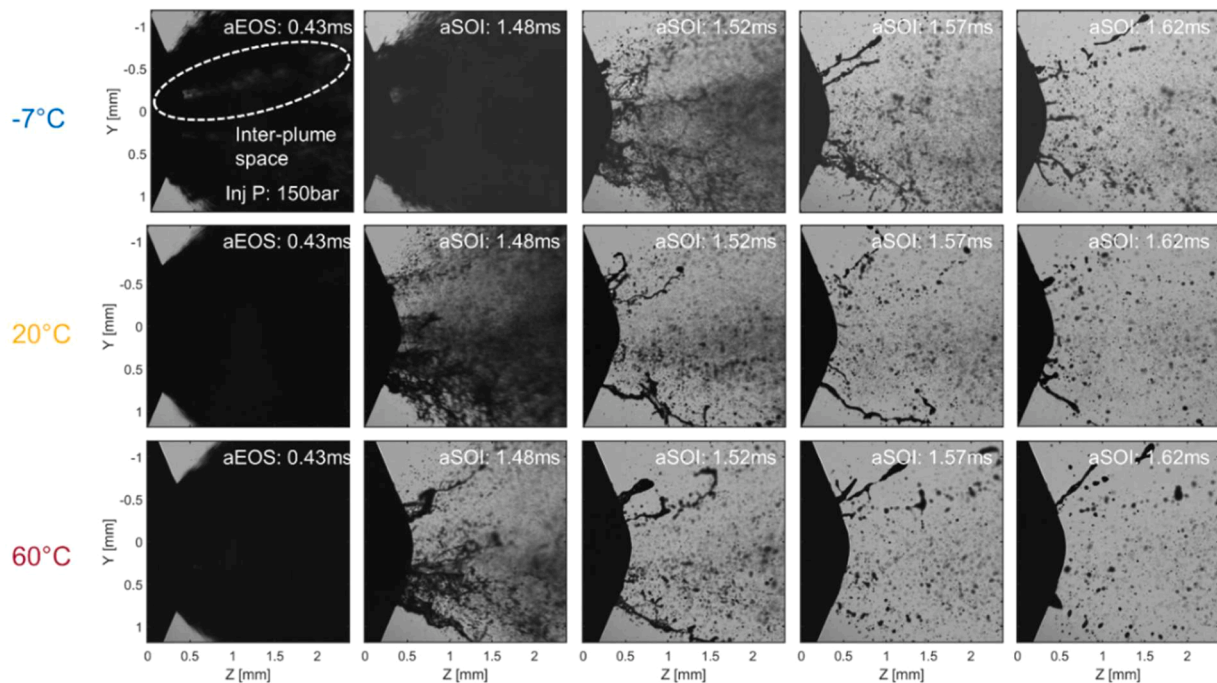

Fig. 11. Microscopic image of near-nozzle spray according to fuel temperature at an injection pressure of 150 bar condition. Time indicates after start of injection, the end of injection is 1.5 ms aSOI (second column).
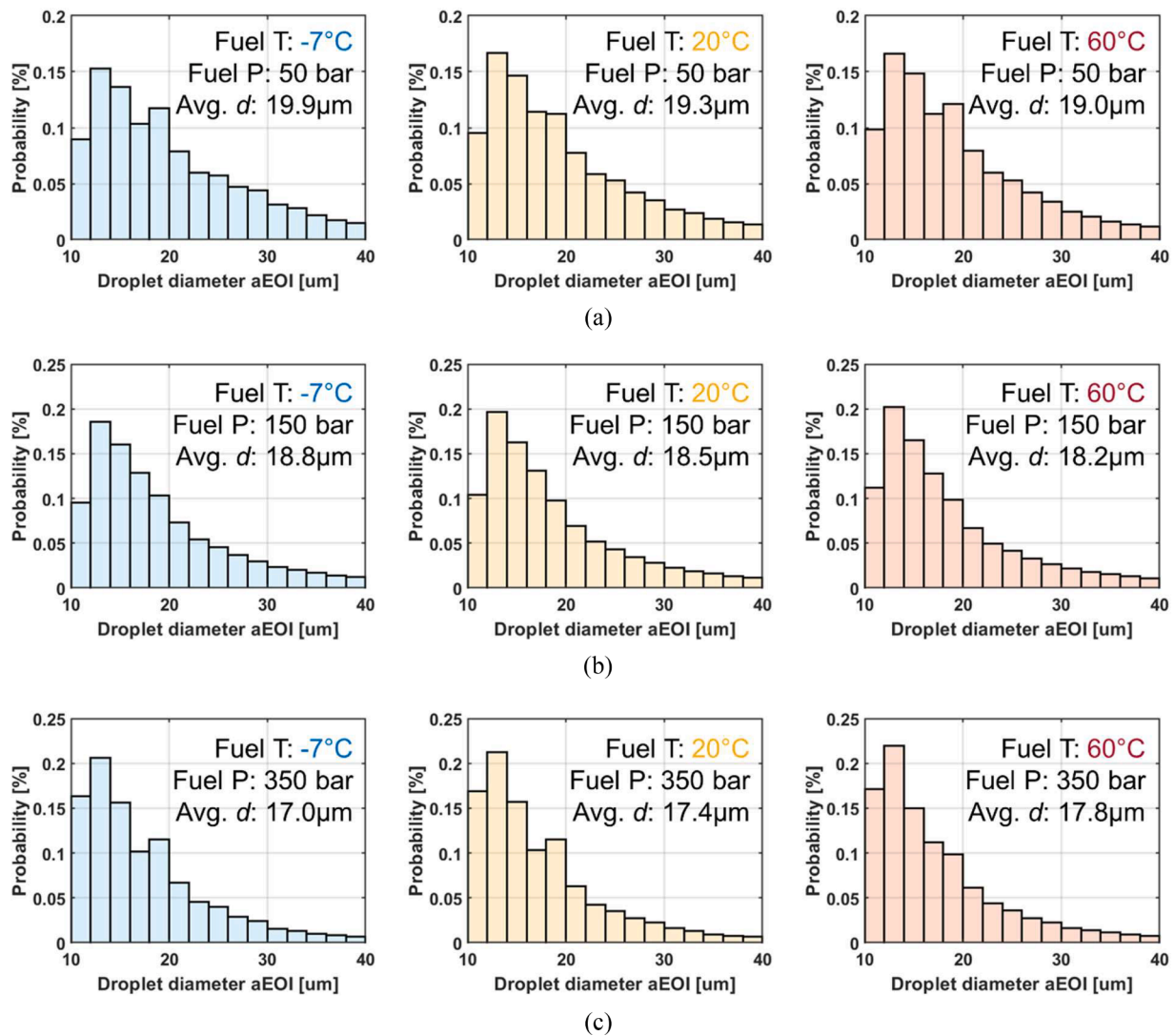
Fig. 12. Droplet size probability according to fuel temperature at (a) 50 bar, (b) 150 bar, and (c) 350 bar conditions. Droplet size was measured at 15 mm from the injector tip, averaged values are presented at right top corner.

hot fuel conditions were reduced when higher injection pressures were applied. However, under an injection pressure of 350 bar, the sprays demonstrated complete plume collapse. This phenomenon can potentially lead to liquid wetting in the combustion chamber, characterized by long liquid penetration lengths and high levels of liquid volume fraction in the spray core region.

- Microscopic spray imaging further confirmed this observation, revealing droplets filling the inter-plume region near the nozzle. Droplet size measurements based on microscopic images did not show significant differences depending on the fuel temperature. However, it is believed that the presence of large droplets under cold start conditions could negatively impact the combustion process.
- In summary, careful calibration of injection timing and the application of moderate injection pressures, along with split injection strategies, are recommended to enhance cold startability and mitigate the potential challenges associated with cold fuel conditions.

Declaration of Competing Interest

The authors declare that they have no known competing financial interests or personal relationships that could have appeared to influence the work reported in this paper.

Data availability

Data will be made available on request.

References

[1] Duronio F, De Vita A, Montanaro A, Villante C. Gasoline direct injection engines – A review of latest technologies and trends. Part 2. Fuel 2020;265:116947. https://doi.org/10.1016/j.fuel.2019.116947.

[2] Zyada A, Zoldak P, Naber J. Development of multiple injection strategy for gasoline compression ignition high performance and low emissions in a light duty engine. SAE Tech Pap 2022:7191. https://doi.org/10.4271/2022-01-0457.

[3] Yamaguchi A, Koopmans L, Helmantel A, Karrholm FP, Dahlander P. Spray characterization of gasoline direct injection sprays under fuel injection pressures

up to 150MPa with different nozzle geometries. SAE Tech Pap 2019. https://doi.org/10.4271/2019-01-0063.

[4] Anbari Attar M, Herfatmanesh MR, Zhao H, Cairns A. Experimental investigation of direct injection charge cooling in optical GDI engine using tracer-based PLIF technique. Exp Therm Fluid Sci 2014;59:96–108. https://doi.org/10.1016/j.expthermflusci.2014.07.020.

[5] Zhang Q, Pei Y, An Y, Peng Z, Qin J, Shi H, et al. Study of water direct injection on knock control and combustion process of a high compression ratio GDI engine. Fuel 2021;306:121631. https://doi.org/10.1016/j.fuel.2021.121631.

[6] Li A, Zheng Z. Effect of spark ignition timing and water injection temperature on the knock combustion of a GDI engine. Energies 2020;13. https://doi.org/10.3390/en13184931.

[7] Duan W, Huang Z, Chen H, Tang P, Wang L, Chen W. Effects of passive pre-chamber jet ignition on combustion and emission at gasoline engine. Adv Mech Eng 2021;13:1–10. https://doi.org/10.1177/16878140211067148.

[8] Wei H, Feng D, Pan M, Pan JY, Rao XK, Gao D. Experimental investigation on the knocking combustion characteristics of n-butanol gasoline blends in a DISI engine. Appl Energy 2016;175:346–55. https://doi.org/10.1016/j.apenergy.2016.05.029.

[9] Yang J, Dong X, Wu Q, Xu M. Effects of enhanced tumble ratios on the in-cylinder performance of a gasoline direct injection optical engine. Appl Energy 2019;236:137–46. https://doi.org/10.1016/j.apenergy.2018.11.059.

[10] Shen K, Xu Z, Chen H, Du J. Combined effects of high energy ignition and tumble enhancement on performance of lean combustion for GDI engine. Exp Therm Fluid Sci 2021;129:110464. https://doi.org/10.1016/j.expthermflusci.2021.110464.

[11] Hwang J, Park Y, Kim K, Lee J, Bae C. Improvement of diesel combustion with multiple injections at cold condition in a constant volume combustion chamber. Fuel 2017;197:528–40. https://doi.org/10.1016/j.fuel.2017.02.049.

[12] Rodriguez JF, Cheng WK. Reduction of cold-start emissions through valve timing in a GDI engine. SAE Int J Engines 2016;9:1220–9. https://doi.org/10.4271/2016-01-0827.

[13] Oh C, Cheng WK. Assessment of gasoline direct injection engine cold start particulate emission sources. SAE Int J Engines 2017;10:1556–65. https://doi.org/10.4271/2017-01-0795.

[14] Yusuf AA, Inambao FL. Effect of cold start emissions from gasoline-fueled engines of light-duty vehicles at low and high ambient temperatures: recent trends. Case Stud Therm Eng 2019;14:100417. https://doi.org/10.1016/j.csite.2019.100417.

[15] Yao C, Zhou T, Yang F, Hu Y, Wang J, Ouyang M. Experimental study of glow plug assisted compression ignition. Fuel 2017;197:111–20. https://doi.org/10.1016/j.fuel.2017.02.008.

[16] Park H, Bae C, Ha C. A comprehensive analysis of multiple injection strategies for improving diesel combustion process under cold-start conditions. Fuel 2019;255:115762. https://doi.org/10.1016/j.fuel.2019.115762.

[17] Mubarak Ali MJ, Hernandez Perez F, Vedharaj S, Vallinayagam R, Dibble R, Im H. Effect of timing and location of hotspot on super knock during pre-ignition. SAE Tech Pap 2017. https://doi.org/10.4271/2017-01-0686.

[18] Gutierrez L, Mansfield AB, Fatouraie M, Assanis D, Singh R, Lacey J, et al. Effects of engine speed on spray behaviors of the engine combustion network "spray G" gasoline injector. SAE Tech Pap 2018:1–7. https://doi.org/10.4271/2018-01-0305.

[19] Bruno BA, Santavicca DA, Zello JV. Fuel injection pressure effects on the cold start performance of a GDI engine. SAE Tech Pap 2003. https://doi.org/10.4271/2003-01-3163.

[20] Payri R, García-Oliver JM, Bardi M, Manin J. Fuel temperature influence on diesel sprays in inert and reacting conditions. Appl Therm Eng 2012;35:185–95. https://doi.org/10.1016/j.applthermaleng.2011.10.027.

[21] Li Z, Pan J, Li W, Wang X, Wei H, Pan J. New insights into abnormal combustion phenomena induced by diesel spray-wall impingement under engine-relevant conditions. Energies 2022;15. https://doi.org/10.3390/en15082941.

[22] Aleiferis PG, Serras-Pereira J, van Romunde Z, Caine J, Wirth M. Mechanisms of spray formation and combustion from a multi-hole injector with E85 and gasoline. Combust Flame 2010;157:735–56. https://doi.org/10.1016/j.combustflame.2009.12.019.

[23] Huang Y, Huang S, Huang R, Hong G. Spray and evaporation characteristics of ethanol and gasoline direct injection in non-evaporating, transition and flash-boiling conditions. Energy Convers Manag 2016;108:68–77. https://doi.org/10.1016/j.enconman.2015.10.081.

[24] Park Y, Hwang J, Bae C, Kim K, Lee J, Pyo S. Effects of diesel fuel temperature on fuel flow and spray characteristics. Fuel 2015;162:1–7. https://doi.org/10.1016/j.fuel.2015.09.008.

[25] Jing D, Zhao H, Li Y, Guo H, Xiao J, Shuai SJ. Numerical investigation on the effect of fuel temperature on spray collapse and mixture formation characteristics in GDI engines. SAE Tech Pap 2018:1–10. https://doi.org/10.4271/2018-01-0311.

[26] Cheng S, Kukkadapu G, Mcnenly M, Saggese C, Curran S, et al. Development of an optimized gasoline surrogate formulation for PACE experiments and simulations overview. 2020. https://www.energy.gov/eere/vehicles/article s/development-optimized-gasoline-surrogate-formulation-pace-experiments-and.

[27] Mcnenly M, Miles P, Som S, Szybist J. Partnership for advanced combustion engines (PACE) – A light-duty national laboratory combustion consortium. Annual Merit Review 2020. https://www.energy.gov/eere/vehicles/articles/partnershi p-advanced-combustion-engines-pace-light-duty-national-0.

[28] Pickett LM, Genzale CL, Manin J. Uncertainty quantification for liquid penetration of evaporating sprays at diesel-like conditions. At Sprays 2015;25:425–52. https://doi.org/10.1615/AtomizSpr.2015010618.

[29] Hwang J, Weiss L, Karathanassis IK, Koukouvinis P, Pickett LM, Skeen SA. Spatio-temporal identification of plume dynamics by 3D computed tomography using engine combustion network spray G injector and various fuels. Fuel 2020;280:118359. https://doi.org/10.1016/j.fuel.2020.118359.

[30] Westlye FR, Penney K, Ivarsson A, Pickett LM, Manin J, Skeen SA. Diffuse back-illumination setup for high temporally resolved extinction imaging. Appl Opt 2017;56:5028. https://doi.org/10.1364/ao.56.005028.

[31] http://www.philiplaven.com/mieplot.htm.

[32] https://ecn.sandia.gov/ecn-workshop/ecn8-workshop/.

[33] Weiss L, Wensing M, Hwang J, Pickett LM, Skeen SA. Development of limited-view tomography for measurement of spray G plume direction and liquid volume fraction. Exp Fluids 2020;61:1–17. https://doi.org/10.1007/s00348-020-2885-0.

[34] Eagle WE, Musculus MPB. Cinema - stereo imaging of fuel dribble after the end of injection in an optical heavy - Duty Diesel engine. In: Proceedings of the THIESEL 2014 conference on thermo- and fluid dynamic processes in direct injection engines; 2014. p. 1–20.

[35] Hwang J, Park Y, Bae C, Lee J, Pyo S. Fuel temperature influence on spray and combustion characteristics in a constant volume combustion chamber (CVCC) under simulated engine operating conditions. Fuel 2015;160:424–33. https://doi.org/10.1016/j.fuel.2015.08.004.

[36] Trost D, Polcar A, Boldor D, Nde DB, Wolak A, Kumbár V. Temperature dependence of density and viscosity of biobutanol-gasoline blends. Appl Sci 2021;11. https://doi.org/10.3390/app11073172.

[37] Tinprabath P, Hespel C, Chanchaona S, Foucher F. Impact of cold conditions on diesel injection processes of biodiesel blends. Renew Energy 2016;96:270–80. https://doi.org/10.1016/j.renene.2016.04.062.

[38] Hwang J, Lee P, Mun S, Karathanassis IK, Koukouvinis P, Pickett LM, et al. Machine-learning enabled prediction of 3D spray under engine combustion network spray G conditions. Fuel 2021;293:120444. https://doi.org/10.1016/j.fuel.2021.120444.

[39] Sun Z, Wang H, Cui M, Nour M, Li X, Xu M. Investigation of flash boiling injection schemes in lean-burn gasoline direct injection engines. Appl Energy Combust Sci 2021;7:100035. https://doi.org/10.1016/j.jaecs.2021.100035.

[40] Dahlander P, Babayev R, Ravi Kumar S, Etikyala S, Koopmans L. Particulates in a GDI engine and their relation to wall-film and mixing quality. SAE Tech Pap 2022:7191. https://doi.org/10.4271/2022-01-0430.

[41] Manin J, Bardi M, Pickett LM, Dahms RN, Oefelein JC. Microscopic investigation of the atomization and mixing processes of diesel sprays injected into high pressure and temperature environments. Fuel 2014;134:531–43. https://doi.org/10.1016/j.fuel.2014.05.060.